Geochemistry, Geophysics, Geosystems®

RESEARCH ARTICLE
10.1029/2024GC011612

Special Collection:
A fresh look at the Caribbean plate geosystems

3D Shear Velocity Structure of the Caribbean—Northwestern South America Subduction Zone From Ambient Noise and Ballistic Rayleigh Wave Tomography

Wenpei Miao[1,2], John Cornthwaite[2], Alan Levander[2], Fenglin Niu[2], Michael Schmitz[3], Guoliang Li[4], Viviana Dionicio[5], and German Prieto[6]

[1]Institute of Geophysics, China Earthquake Administration, Beijing, China, [2]Department of Earth, Environmental and Planetary Science, Rice University, Houston, TX, USA, [3]Fundación Venezolana de Investigaciones Sismológicas (FUNVISIS), Caracas, Venezuela, [4]Department of Earth Sciences, Southern California Earthquake Center, University of Southern California, Los Angeles, CA, USA, [5]Servicio Geológico Colombiano, Bogotá, Colombia, [6]Departamento de Geociencias, Universidad Nacional de Colombia, Bogotá, Colombia

Abstract The Caribbean-South America subduction zone is a flat subduction zone, with Laramide-style thick-skinned uplifts occurring in the Merida Andes, Sierra de Perija Range, and Santa Marta Massif. Geodetic measurements and historical seismicity show this region is storing strain energy and is capable of a mega-thrust earthquake ($M \geq 8.0$). Previous seismic investigations of the lithosphere and upper mantle in this area are either very large scale, very local, or only peripheral to this area; therefore, details of the Caribbean plate subduction geometry beneath the Maracaibo block remain unclear. In this study, we used a new data set acquired by the Caribbean-Merida Andes seismic experiment (CARMA), which comprised 65 temporary broadband stations and 44 permanent stations from the Colombian and Venezuelan national seismic networks. We jointly inverted ambient noise Rayleigh wave Z/H ratios, phase velocities in the 8–30 s band and ballistic Rayleigh wave phase velocities in 30–80 s band to construct a 3-D S-wave velocity model in the area between 75°–65°W and 5°–12°N. The 3-D model reveals a general increase in crust thickness from the trench to the southeast. An anomalous area is the Lake Maracaibo, which is underlaid by the thinnest crystalline crust in the region. This observation may indicate that the Maracaibo block is experiencing a contortion deformation within the crust. We also identified a high velocity anomaly above the subducting Caribbean slab, likely representing a detached piece of eclogitized Caribbean large igneous province from the base of the Maracaibo block. Additionally, our V_s model clearly indicates a slab tear within the subducted Caribbean slab, approximately beneath the Oca-Ancon Fault.

Plain Language Summary The Caribbean-South America subduction zone is a flat subduction zone that the South-American plate subducts beneath the Maracaibo block, which can lead to destructive earthquakes ($M \geq 8.0$) due to built-up strain. This study used data from the Caribbean-Merida Andes seismic experiment (CARMA), which included 65 temporary and 44 permanent seismic stations in Colombia and Venezuela, to build a 3-D S-wave velocity model. The model shows the crust thickens from the trench toward southeast, with the thinnest crust under Lake Maracaibo, indicating significant deformation in the Maracaibo block. The study also found high-speed anomalies above the subducting plate, suggesting a detached fragment of the Caribbean large igneous province beneath the Maracaibo block. Additionally, a slab tear was identified beneath the Oca-Ancon Fault, which could impact seismic activity in the region. These findings enhanced our understanding of the region's tectonic processes and potential earthquake risks.

Key Points:

- The Maracaibo block is experiencing a contortion deformation within the crust
- High velocity anomalies above the subducting Caribbean slab indicate a detached piece of eclogitized Caribbean large igneous province
- A slab tear within the subducted Caribbean slab is found approximately beneath the Oca-Ancon Fault

Supporting Information:

Supporting Information may be found in the online version of this article.

Correspondence to:

W. Miao,
miaowp@cea-igp.ac.cn

Citation:

Miao, W., Cornthwaite, J., Levander, A., Niu, F., Schmitz, M., Li, G., et al. (2024). 3D shear velocity structure of the Caribbean—northwestern South America subduction zone from ambient noise and ballistic Rayleigh wave tomography. *Geochemistry, Geophysics, Geosystems*, *25*, e2024GC011612. https://doi.org/10.1029/2024GC011612

Received 15 APR 2024
Accepted 28 AUG 2024

Author Contributions:

Conceptualization: John Cornthwaite, Alan Levander, German Prieto
Data curation: Michael Schmitz, Viviana Dionicio, German Prieto
Formal analysis: Wenpei Miao, John Cornthwaite
Funding acquisition: Alan Levander, Fenglin Niu

1. Introduction

Flat-slab subduction occurs at ∼10% of modern subduction zones, including several flat subduction zones along the western South American (SA) margin (Gutscher et al., 2000). Geological evidence suggests that ∼70% of the SA margin experienced flat subduction in the Cenozoic (Gutscher et al., 2000; Ramos & Folguera, 2009). Flat subduction zones share several features, such as overriding plate deformation that is far from the trench (e.g., Bird, 1988; Humphreys et al., 2003; Jordan & Allmendinger, 1986), and volcanism that is either far from the trench or absent altogether (Bishop et al., 2017; Eakin et al., 2014; Kay et al., 1987). These features are distinct from normal subduction (Barazangi & Isacks, 1976; Ben-Avraham et al., 1981; Ramos et al., 2002). Many flat

Methodology: Guoliang Li
Project administration: Alan Levander, Fenglin Niu
Resources: Viviana Dionicio
Supervision: Alan Levander, Fenglin Niu
Visualization: Wenpei Miao, John Cornthwaite
Writing – original draft: Wenpei Miao
Writing – review & editing: Alan Levander, Fenglin Niu

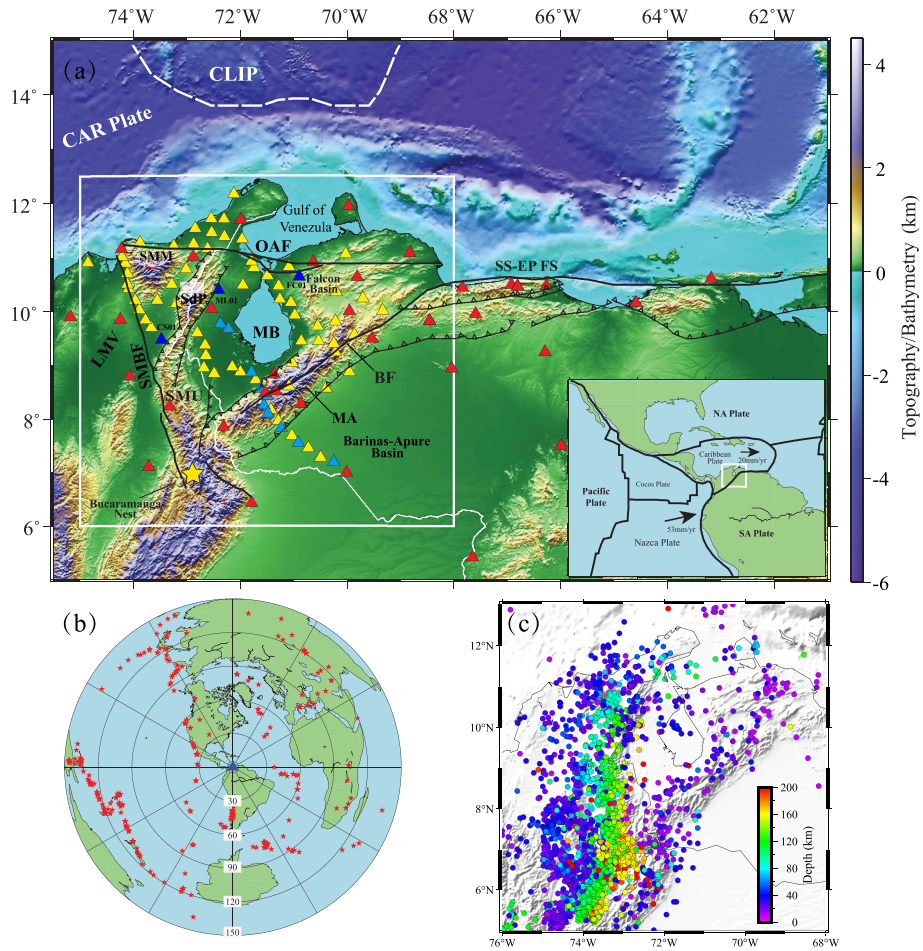

Figure 1. (a) Map of the study area with the main surface geology structure included. Red triangles represent 32 permanent stations in Columbian and Venezuelan national seismic networks, yellow and blue triangles represent 65 broadband temporary stations, and cyan triangles represent 12 broadband stations from the GIAME project in Venezuela, combined as the CARMA Array. Due to the irregular distributions of seismic stations, the main resolution is located in the area bounded by a white box. The lower right corner inset shows relative plate motions around the Caribbean and South America plate (C. Wang et al., 2019; Zhang et al., 2017). CAR, the Caribbean plate; CLIP, Caribbean Large Igneous Province; SMM, Santa Marta Massif; SdP, Sierra de Perija Range; OAF, Oca-Ancon Fault; SMBF, Santa Marta-Bucaramanga Fault; BF, Bocono Fault; MA, Merida Andes; MB, Maracaibo Basin; SMU, Santander Massif Uplift; LMV, Lower Magdalena Valley Basin; SS-EP FS, San Sebastian-El Pilar Fault Systems. (b) Azimuthal equidistant projection map displaying earthquakes selected for two-plane-wave tomography. The chosen earthquakes have epicentral distances ranging from 30° to 150° and magnitudes between 5.6 and 7.0. (c) Map depicting local seismicity compiled from earthquake catalogs issued by the International Seismological Center and the Servicio Geológico Colombiano.

slab segments are narrow compared to the subducted plate length, and their presence leads to tears or deformation in the subducting plate.

The Caribbean plate (CAR) collided with and initiated subduction beneath northwestern SA at about 60–55 Ma as the American plates moved westward (Cardona et al., 2011; Mora et al., 2017). The complex oblique collision led to the development of large-scale strike slip systems and a series thrust belts in northernmost SA as the buoyant Caribbean large igneous province (CLIP) was overridden by the Maracaibo block following a period of more normal subduction (Duerto et al., 2006; Montes et al., 2019; Mora et al., 2017; Taboada et al., 2000). Flat subduction resulted in the Eocene uplift of the Santa Marta Massif (SMM), late Eocene-Miocene uplift of the Sierra de Perija (SdP), and mid to late Miocene uplift of the Merida Andes (MA), as shown in Figure 1 (Kellogg & Bonini, 1982; Pennington, 1981). Similar to other flat subduction zones, the overriding Maracaibo block lithosphere has experienced basement-involved Laramide-style thrusting, has lacked magmatism since 45 Ma, and is seismically active over a broad area (Cardona et al., 2011; Mora et al., 2017; Taboada et al., 2000). Analysis of

earthquakes and GPS data show that along most of the Caribbean-South American (CAR-SA) boundary, the dominant CAR motion is 20 mm/yr almost due east with respect to SA, whereas in northwestern SA the CAR-SA motion is 20 mm/yr in an E-SE direction (Audemard, 2001; Audemard & Castilla, 2016; Audemard et al., 2005; Hippolyte & Mann, 2011). Therefore, western Venezuela is undergoing present-day northwest to southeast shortening associated with subduction of the CAR under SA (Colmenares & Zoback, 2003; Kellogg, 1984; Mann et al., 2006).

The ranges and the Maracaibo Basin (MB) together form the triangular Maracaibo block (Figure 1), a deforming lithospheric fragment bounded by strike slip systems that is caught between CAR subduction in the west and northwest, and CAR strike slip to the north (Kellogg & Bonini, 1982; Symithe et al., 2015). The SMM and the SdP occupy the northwestern corner of the Maracaibo block and are truncated to the north by the Oca-Ancon right lateral strike-slip system with a slip rate of ∼2 mm/yr (Audemard, 2009; Audemard & Audemard, 2002; Audemard & Castilla, 2016). Separating the SdP from the MA is the MB, which formed as a passive margin along western SA in the Jurassic and evolved into a foreland basin during Cenozoic convergence (Mann et al., 2006). The left-lateral Santa Marta-Bucaramanga fault (SMBF) and Santander Massif Uplift (SMU) form the western boundary of the Maracaibo block; the right lateral Bocono Fault (BF) running along the axis of the MA forms its eastern boundary (Audemard, 2003; Symithe et al., 2015).

The Maracaibo block is currently escaping northward relative to the SA plate over both the subducting CAR plate in the northwest, and the nonsubducting CAR plate in the north (Audemard, 2009). The Oca-Ancon Fault (OAF) is a right-lateral strike-slip fault with a ∼2 mm/yr slip rate whose motion has largely been taken up along the more recently formed BF (Audemard, 2009, 2014; Escalona & Mann, 2006; Kellogg, 1984), which merges eastward with the active right lateral San Sebastian-El Pilar fault systems (SS-EPFS) of central and eastern Venezuela (Schubert, 1982).

Several large basins rich in hydrocarbons are located within this region. Prior to Paleocene CAR-SA plate interactions, sediments were deposited along passive continental margins in western South America (De Toni & Kellogg, 1993; Duerto et al., 2006; Macellari, 1995). Starting in the northeastern corner of our study region (Figure 1), the inland Falcon Basin experienced an N-S crustal extension due to the CAR-SA compression (Audemard, 2001). It was a depocenter from the late Eocene to the middle Miocene when it was inverted and uplifted to a mean elevation of 1,500 m (Audemard, 2001; Bezada et al., 2008). The MB, bounded by the SdP Range to the northwest, the MA in the southeast and the Falcon Basin in the northeast, is filled with sediments of Middle Mesozoic—Quaternary age and covers a large part of the Maracaibo block (Audemard & Audemard, 2002; Mann et al., 2006). The Lower Magdalena Valley Basin, located southwest of the SMBF, formed from the Oligocene to the recent. It is considered to be part of the forearc basin system developed during CAR subduction beneath continental SA (Audemard, 2003; Audemard & Audemard, 2002; Boschman, 2021; Syracuse et al., 2016). On the southeast flank of the MA, the Barinas-Apure Basin is a foreland basin that formed due to lithospheric flexure and sediment transport during the MA uplift (Schmitz et al., 2021).

Previous geodetic studies have suggested that this region has potential for a megathrust ($M \sim 8+$) earthquake associated with it (Bilham & Mencin, 2013). Significant destructive earthquakes have been recorded along the BF in Venezuela (Audemard & Audemard, 2002). The current seismic activity in the region remains high, with the majority of shallow earthquakes concentrated along the SMBF system, followed by the BF system (Figure 1c). In contrast, the OAF exhibits minimal seismic activity, with very few recorded earthquakes. Earthquakes associated with subduction are traceable to depths of up to 200 km. Although this geographic area is relatively small, the SMM, SdP, and MA reach highest elevations of 5,710, 3,630, and 4,981 m, respectively. The SMM is of particular interest as its large free air and Bouguer gravity anomalies (Arnaiz-Rodríguez & Audemard, 2014; Sandwell & Smith, 2009) indicate that it is out of isostatic equilibrium and is likely supported by the subducting CAR.

Although many petroleum-related seismic surveys have been conducted in this area, details of the subduction geometry of the CAR plate beneath the Maracaibo block have only recently begun to be understood (Cornthwaite et al., 2021; Sun et al., 2022). Earlier seismic investigations of the lithosphere and upper mantle are either very large scale, very local, or only peripheral to this area (Avila-García et al., 2022; Barrera-Lopez et al., 2022; Bezada et al., 2010; Hilst & Mann, 1994; Masy et al., 2015; Mazuera et al., 2019; van Benthem et al., 2013). Here we present a shear velocity model of northwestern South America made from Rayleigh waves recorded by the 2016–2018 CARibbean-Mérida Andes (CARMA) broadband seismic experiment. To investigate this complex region, we jointly inverted ambient noise Rayleigh wave Z/H ratios, phase velocities in the 8–30 s band and

ballistic Rayleigh wave phase velocities in the 30–80 s band to construct a 3-D S-wave velocity model in the area from 75°–65°W to 5°–12°N. Rayleigh wave *Z*/*H* ratios are sensitive to the shallow sedimentary structure, while the phase velocity data have good depth resolutions of the crust and upper mantle.

2. Data and Methods

2.1. CARMArray

The data used in this study were acquired by the CARMA seismic deployments that comprised 65 IRIS-PASSCAL broadband stations deployed from April 2016 to March 2018, 12 broadband stations from the GIAME project in Venezuela, and 32 broadband stations from the national seismic networks of Venezuela and Colombia. Hereafter, we refer to it as the CARMArray (Levander, 2016). The 109 stations covered an area of ∼1,300 km by 600 km, with the area of best resolution extending from the Caribbean coast of northeast Colombia to the MA of west Venezuela (≤68°W) (white box in Figure 1).

In this study, we first extracted Rayleigh wave *Z*/*H* ratios and phase velocities in the period range of 8–30 s from daily continuous ambient noise data. We also measured phase velocities in the periods between 30 and 80 s from ballistic Rayleigh waves, that is, Rayleigh waves from teleseismic events, using the two-plane-wave method (Forsyth & Li, 2005; Yang & Forsyth, 2006b). Then, we employed a Markov Chain Monte Carlo (MCMC) method to jointly invert these data to construct a 3D S-wave velocity model in the area from 75°–65°W to 5°−12°N.

2.2. Extracting Rayleigh Wave Phase Velocities and *Z*/*H* Ratios From Ambient Noise Data

For three-component ambient noise data, we followed the data processing procedures of Bensen et al. (2007), Lin et al. (2014), and Li et al. (2016). First, we collected three-component continuous ambient noise data from the 109 CARMA stations over their entire deployment periods. Second, we cut the continuous data into daily segments and removed instrument responses, linear trends, and means. Then, the data were bandpass filtered in the frequency band of 0.02–0.5 Hz and decimated to one sample per second. Third, for each station, we used the same temporal normalization and spectral whitening for all three-component data in order to retain the amplitude ratio between the three components. After that, we calculated the nine-component cross-correlation functions (CCFs) between all station pairs with overlapping times, i.e., ZZ, ZE, ZN, EE, EN, EZ, NN, NE, and NZ.

Rayleigh wave phase velocities are extracted from ZZ CCFs. To improve the signal-to-noise ratio (SNR) of the Rayleigh wave arrivals, we employed a two-step stacking strategy. The first step is storing the daily CCFs in chronological order and linearly stacking them every 5 days. We then employed the time-frequency phase weight stacking (tf-PWS) method to stack these 5-day linearly stacked CCFs (Li et al., 2018). The tf-PWS, based on the frequency inverse S transform, has been proved to be more effective in enhancing SNR while retaining the dispersive characteristics of stacked waveforms (Li et al., 2018). We folded the CCFs and stacked the causal and acausal segments to create the so-called symmetrical CCFs. Dispersion curves between station pairs are extracted from symmetrical CCFs with an SNR ≥ 8 using automated frequency-time analysis (e.g., Dziewonski et al., 1969; Levshin & Ritzwoller, 2001). Using ray theory, we inverted the measured phase velocities between all station pairs to construct phase velocity maps (Figures 3a–3d). The inversion was performed with a grid size of 0.25° by 0.25°.

To measure the Rayleigh wave *Z*/*H* ratios, we adopt the method elaborated by Li et al. (2021) and Miao et al. (2022), and briefly describe the main steps here. We separated the positive and negative parts of each CCF as they reflect different structures and used the linear method to stack them. Then, the stacked nine-component CCFs are rotated to the radial (*R*) and transverse (*T*) directions. An example of the calculated CCFs between station pair CS01 and FC01 is shown in Figure 2a. For a station pair of A and B, the *Z*/*H* ratio for a given period at station B can be estimated from

$$ZH(T) = \frac{Z_A Z_B}{Z_A R_B} = \frac{R_A Z_B}{R_A R_B} = \frac{Z_B Z_A}{R_B Z_A} = \frac{Z_B R_A}{R_B R_A} = \frac{Z_{\text{stack}}}{R_{\text{stack}}} \quad (1)$$

where

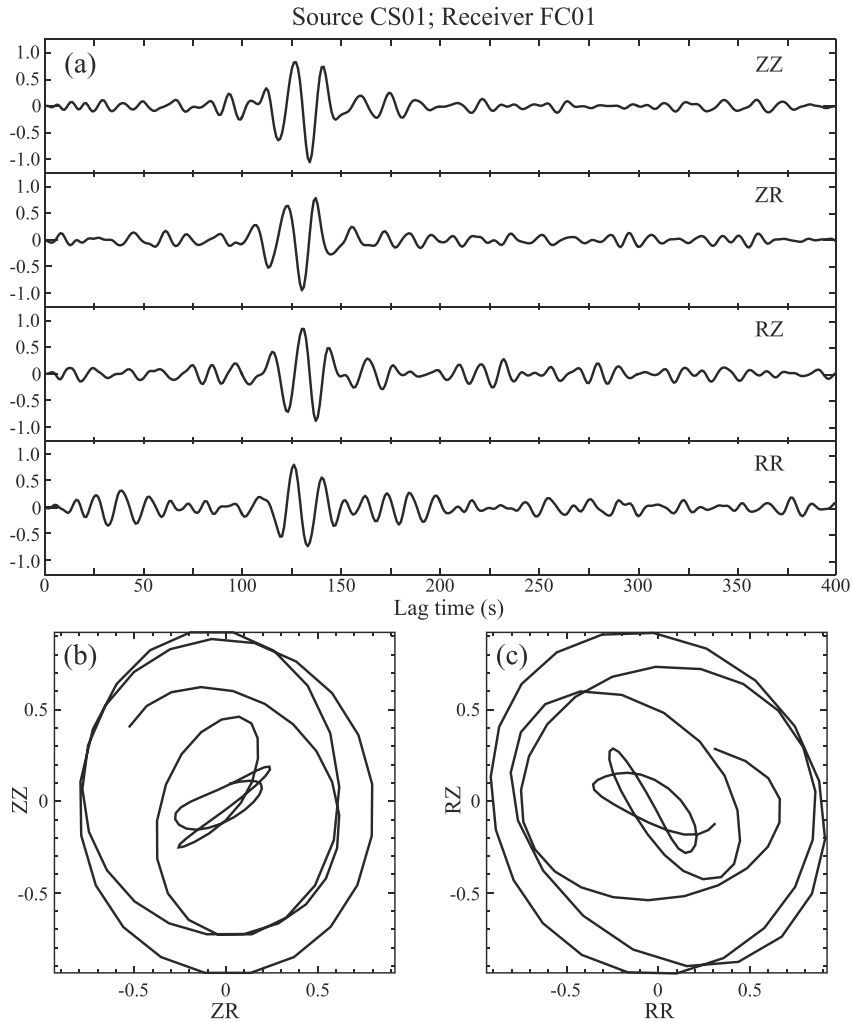

Figure 2. An example of the calculated cross-correlation functions (CCFs) and observed Rayleigh wave particle motions. (a) ZZ, ZR, RZ and RR cross-correlation functions between stations CS01 and FC01. CS01 is the source station and FC01 is the receiver station. (b) Particle motions beneath the station FC01 that derived from ZZ and ZR cross-correlation functions. (c) Same as (b), except from RZ and RR cross-correlation functions.

$$Z_{\text{stack}} = Z_A Z_B + iH[R_A Z_B] + Z_B Z_A + H[Z_B R_A]$$
$$R_{\text{stack}} = H[Z_A R_B] + R_A R_B + iH[R_B Z_A] + R_B R_A \quad (2)$$

Here, the first letter indicates the component of source, and the second letter represents the component of receiver. The subscripts denote the names of stations, with the first and second ones acting as the virtual source and receiver, respectively. For example, $Z_A R_B$ represents the Green's function recorded on the radial component of station B from a vertical impulse source at station A. Operation *H[]* and *iH[]* result in 90° phase delay or phase advance for a given waveform to correct the 90° phase difference between different components. After the phase calibrations, the eight CCFs in Equation 2 are expected to be in-phase for Rayleigh waves and were further stacked to increase the SNR of Z_{stack} and R_{stack}. The stacked vertical and radial component Rayleigh waves were narrow bandpass filtered to compute *Z/H* ratios at different periods. For each set of filtered Z_{stack} and R_{stack}, we calculated their zero-lag cross-correlation coefficient and discarded pairs with coefficients less than 0.8. We finally computed the envelope functions of the filtered Z_{stack} and R_{stack} and took the ratio of their maximum amplitudes as the *Z/H* ratio. For each targeted station, we computed the *Z/H* ratios of all possible pairs and took their average as the final estimate of the *Z/H* ratio. An example of calculated ZZ, ZR, RZ, and RR CCFs between

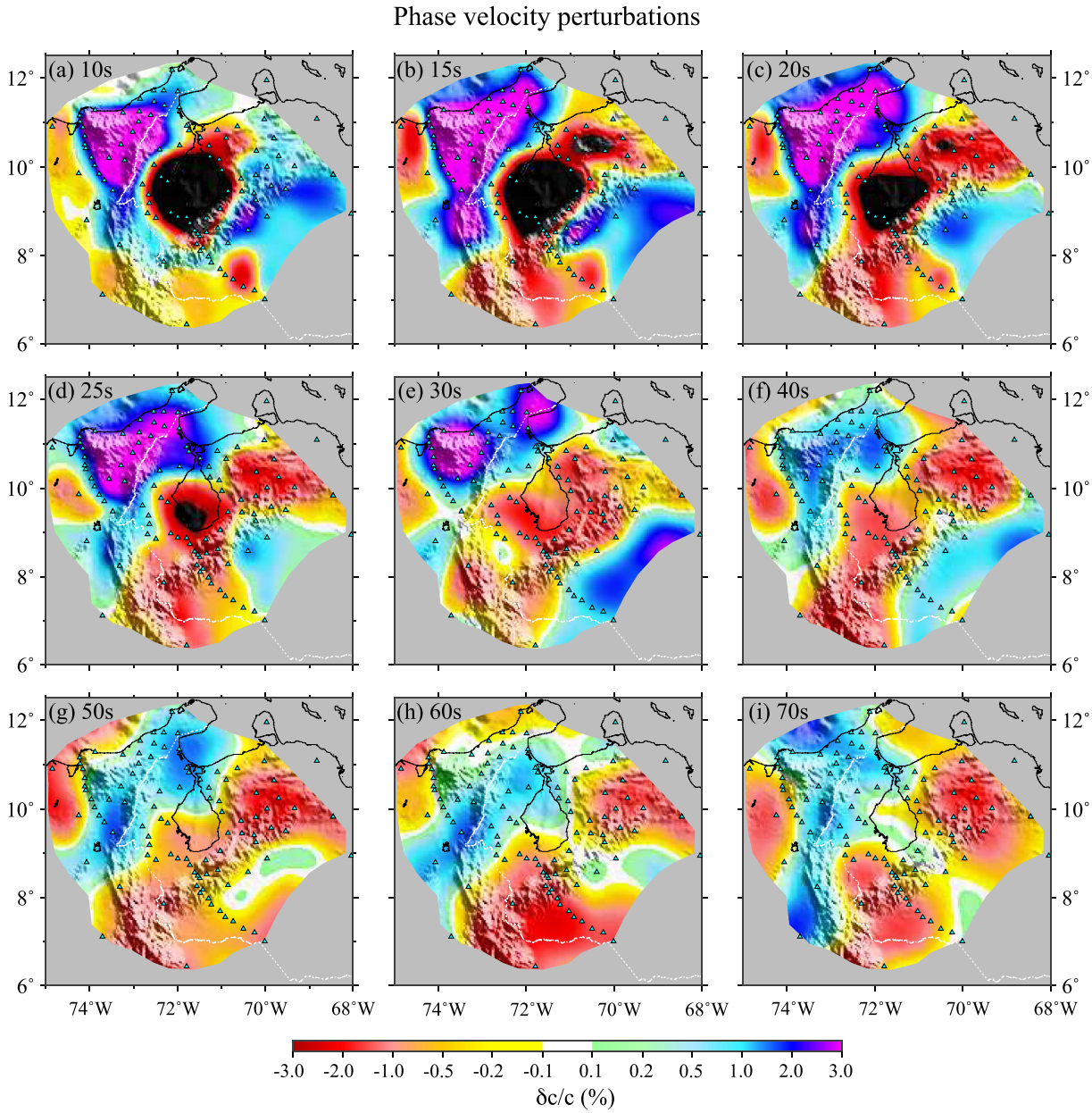

Figure 3. Rayleigh wave phase velocity perturbation maps derived from ambient noise and ballistic data. Panels (a–d) show Rayleigh wave phase velocity perturbation measured from ambient noise data at periods of 10, 15, 20, and 25 s, respectively. Panels (e–i) display Rayleigh wave phase velocity perturbation measured from ballistic data at periods of 30, 40, 50, 60, and 70 s, respectively.

the stations CS01 and FC01 is shown in Figure 2a, and the elliptical particle motions are shown in Figures 2b and 2c.

2.3. Extracting Rayleigh Wave Phase Velocity From Ballistic Data

Since we required station spacing to be greater than two wavelengths when we selected ambient noise CCFs, we were able to obtain robust phase velocity and *Z*/*H* ratio measurements only in the period band of 8–30 s. To obtain phase velocities at longer periods (30–80 s), we employed Rayleigh waves of teleseismic earthquakes and applied the two-plane-wave method to compute velocities across the 2-D array (e.g., Forsyth & Li, 2005; Yang & Forsyth, 2006a, 2006b). This method considers multipathing effects of the incoming wavefield and applies finite-frequency amplitude and phase sensitivity kernels to improve lateral resolution (Yang & Forsyth, 2006b). We

analyzed data from a total of 325 earthquakes located within a distance range of 30° to 150° from the array. These earthquakes were selected from the International Seismological Center catalog with magnitudes ranging from 5.6 to 7.0, occurring between April 2016 and March 2018 (Figure 1b).

2.4. Markov Chain Monte Carlo Joint Inversion

We first obtained the phase velocity dispersions at each station by linearly interpolating values taken from its surrounding four grid points based on their distances to each station. Then, we jointly inverted the phase velocities and *Z/H* ratios that measured at each station to obtain a 1-D S-wave velocity model beneath each station using the MCMC method described in Bodin et al. (2012), Afonso et al. (2013), Shen et al. (2013), and Li et al. (2016).

The likelihood function in the joint inversion is defined by

$$p(d_{\text{obs}}|m) = \frac{1}{S} e^{-\frac{1}{2}M_{\text{joint}}(m)}, \tag{3}$$

where S is a normalization parameter, and the joint misfit function $M_{\text{joint}}(m)$ is defined by

$$\begin{aligned} M_{\text{joint}}(m) &= M_{PH}(m) + M_{ZH}(m) \\ &= \frac{1}{N}\sum_{i=1}^{N}\frac{\left[PH_i(m) - PH_i^{\text{obs}}\right]^2}{\sigma_1^2} + \frac{1}{M}\sum_{j=1}^{M}\frac{\left[ZH_j(m) - ZH_j^{\text{obs}}\right]^2}{\sigma_2^2}. \end{aligned} \tag{4}$$

Here, PH_i^{obs} and ZH_j^{obs} are the observed phase velocities and *Z/H* ratios, while $PH_i(m)$ and $ZH_j(m)$ represent the calculated phase velocities and *Z/H* ratios at the *i*th and *j*th periods of a trial model generated by the Monte Carlo method. N and M are the number of periods of phase-velocity and *Z/H* ratio measurements, respectively. Since uncertainties (σ_1, σ_2) in these two types of data sets are usually difficult to determine, we treated them as unknown parameters, which were also inverted in the joint inversion. For a given trial model, we used the method from Computer Programs in Seismology (Herrmann & Ammon, 2004) to compute the theoretical Rayleigh wave phase velocities and *Z/H* ratios.

We divided the 1-D velocity model beneath each station into three layers: a sedimentary layer, a crystalline crust layer, and an upper mantle layer. We assumed *Vs* in the sedimentary layer increases linearly with depth; therefore *Vs* within the sediments is determined by three parameters: *Vs* at the top, *Vs* at the bottom, and the layer thickness. We employed B-splines to represent *Vs* variations over depth in the crystalline crust and the upper mantle layers. We used a total of five independent parameters to determine the crystalline crust, including four B-spline coefficients and a Moho depth, and four B-spline coefficients for *Vs* in the upper mantle. As the Rayleigh wave *Z/H* ratio has sensitivities of the *Vp* in shallow depth (Lin et al., 2012), the *Vp* in the sedimentary layer is also inverted. Thus, each 1-D model had a total of 13 independent parameters, which were perturbed in wide depth and velocity ranges.

The data sets are not sensitive to the density and *Vp* in the crystalline crust and mantle; therefore, we use the Brocher's Law (Brocher, 2005) to scale the density and *Vp* from *Vs*. The density values in the sedimentary layer are calculated using Gardner's relation (Gardner et al., 1974). Since the longest period of Rayleigh waves that we used in this study is 80 s, we only inverted the S-wave velocity structure from earth's surface to 150 km depth (Yang & Forsyth, 2006b). We kept the PREM (Preliminary Reference Earth Model, Dziewonski & Anderson, 1981) *Vs* in the depth range of 150–200 km and used a constant *Vs* below 200 km. The 1-D model included attenuation parameters (Q_p and Q_s), which were also taken from the PREM model.

3. Results

Here, we describe measured dispersion curves extracted from ambient noise data and ballistic data. Then, we introduce the measured *Z/H* ratios from ambient noise Rayleigh wave data and the inverted 3-D V_s model in this study.

3.1. Phase Velocity Maps

Figures 3a–3d show Rayleigh wave phase velocities extracted from ambient noise at periods of 10, 15, 20, and 25 s, while Figures 3e–3i represent the phase velocities extracted from earthquake data at periods of 30, 40, 50, 60, and 70 s. The dispersion from ambient noise and ballistic data overlap at 30 s, their comparison is shown in Figure S1 in Supporting Information S1. In general, these two phase-velocity maps are consistent with each other, and the ambient noise phase velocity is an average of 0.34 ± 0.95% higher than the ballistic data phase velocity average (Figure S1d in Supporting Information S1). We also ran checkerboard tests and found that the raypath coverage resolved anomalies with a size greater than 0.25° × 0.25° (Figure S2 in Supporting Information S1). In Figure 3, we have clipped the areas that lack good resolution based on the results of checkerboard tests.

For short periods 10–25 s (Figures 3a–3d), strong low phase velocity anomalies (>3%) are located inside the MB, consistent with thick low seismic velocity sediments. High phase velocity anomalies are located beneath the SdP Range, SMM and MA. At the intermediate periods, 30–40 s (Figures 3e and 3f), high phase velocity anomalies persist beneath the SMM and SdP Range, while low phase velocity anomalies are observed under the MA, the Falcon Basin and Bucaramanga region. They likely reflect relatively thick continental crust beneath these areas. At 50–60 s (Figures 3g and 3h), we observe bands of 0.5%–1.5% high velocities in the northwest that are orthogonal to the subduction direction, while at 70 s this anomaly is elongated to the southwest from the SdP Range to the Bucaramanga region.

3.2. Rayleigh Wave *Z*/*H* Ratios

To retain the most reliable *Z*/*H* ratio measurements, we only selected the Rayleigh waves recorded on both the *Z* and *R* components with a SNR >5, and station pairs that are more than two wave-lengths apart. Figure 4 shows *Z*/*H* ratio maps at 10, 15, 20, and 25 s by interpolating the measurements from 94 stations. Since the *Z*/*H* ratios are most sensitive to shallow structures, low *Z*/*H* ratios are registered at stations in sedimentary basins, while high *Z*/*H* ratio anomalies are found at stations installed in mountainous regions. At 10 s (Figure 4a), high *Z*/*H* ratio values are seen in the SMM, SdP Range and MA. Low *Z*/*H* ratio values are located in the MB and the Barinas-Apure Basin areas. The *Z*/*H* ratio at 10 s is mostly sensitive to velocity structure in the top 5 km, and a low *Z*/*H* ratio is generally caused by sediments with low seismic velocity. The MB, filled with Miocene and Pliocene marine deposits, shows a low *Z*/*H* ratio of 0.6–0.8. The Falcon Basin with deep marine deposition shows a moderate *Z*/*H* ratio of 0.8–1.2. Our measured *Z*/*H* ratios are generally consistent with surface geology. However, as the periods increase, the contrasts between the low and high *Z*/*H* ratios become smaller due to decreasing sensitivity of longer period *Z*/*H* ratios with deeper structures.

3.3. 3-D V_s Model

We jointly inverted Rayleigh wave phase velocities from ambient noise and ballistic data, and the *Z*/*H* ratios from ambient noise data for a 1-D V_s model beneath each station using the joint inversion method described in Section 2.4. To better construct the three-dimensional shear wave velocity structure within the study area, we applied a two-step inversion strategy. First, we jointly inverted the Rayleigh wave phase velocities and *Z*/*H* ratios from ambient noise data, which are phase velocities of 8–30 s and *Z*/*H* ratio of 8–25 s, to obtain shallow velocity structures. Then, we fixed the shallow velocity structures and inverted the longer period phase velocities only to construct deeper *Vs* structures. Following this two-step inversion strategy, we obtained a 1-D V_s model that extends to 150 km depth beneath each station. Our synthetic analysis demonstrated that this two-step inversion approach reduces non-uniqueness and provides better constraints on the 1-D velocity models. As an example, the joint inversion at station CS01 shown in Figure 5 indicates that the inversion model fits both the phase-velocity and *Z*/*H* ratio data. The posterior density functions suggest that sediment thicknesses are well constrained (Figure 5d), while the Moho depth range is wider as it is only constrained by phase velocity data. We interpolated all 1-D V_s profiles onto a 0.25 × 0.25-degree grid using a minimum curvature surface fitting method to construct the final 3-D V_s model. Because the interpolation was based on *Vs* values at each depth, information on sediment and crust thickness is not available at each grid point. To resolve this, we first determined the *Vs* value at the Moho beneath each station, which was approximately 4.2 km/s. We then used this value to estimate the Moho depth across the grids.

Figure 6 shows the map view of shear velocities at eight different depths. Velocity perturbations of two depths are also shown in Figure S3 in Supporting Information S1. At 1 km depth, the MB, Lower Magdalena Valley Basin,

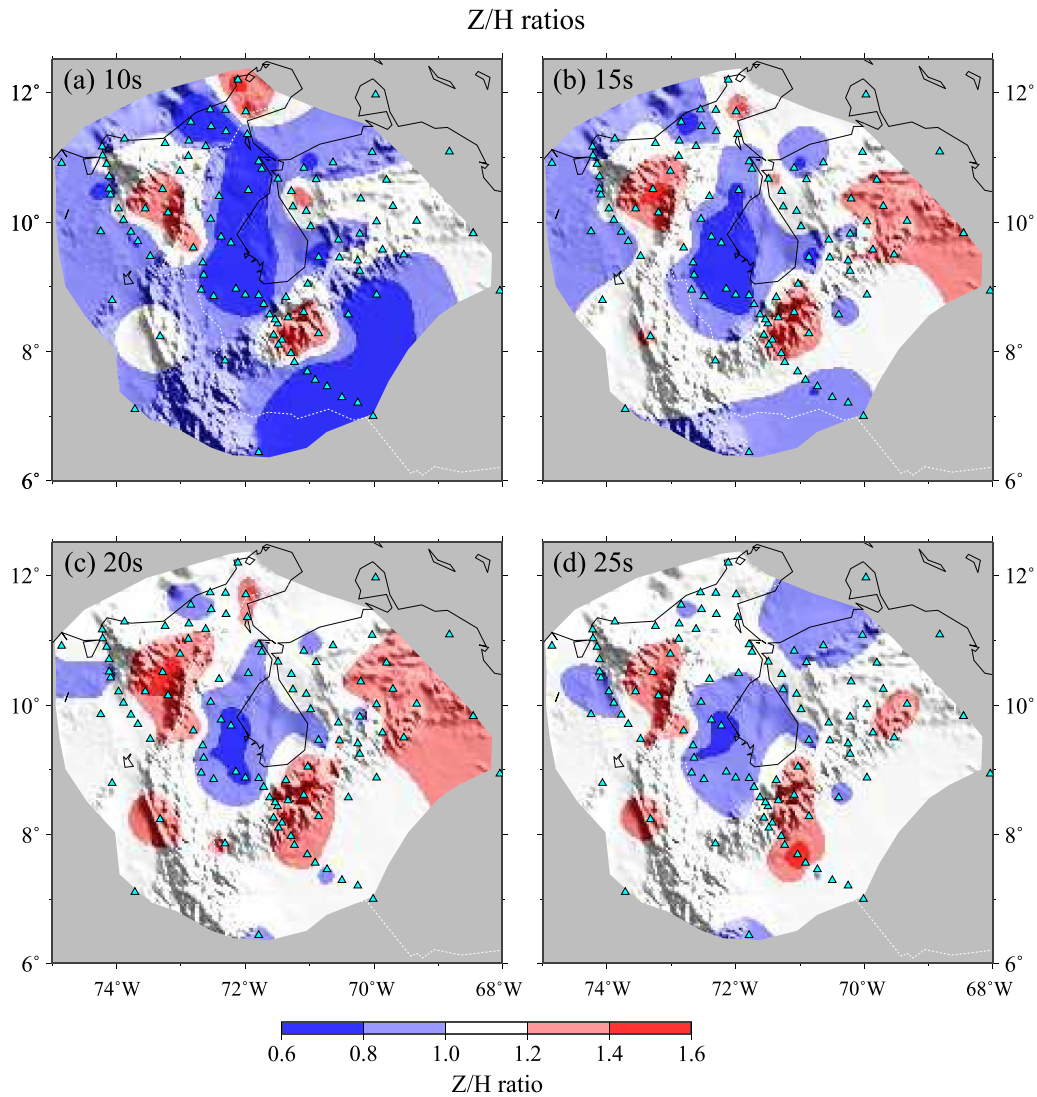

Figure 4. Map showing Rayleigh wave *Z/H* ratios measured at periods of (a) 10 s, (b) 15 s, (c) 20 s, and (d) 25 s, respectively.

Barinas-Apure Basin, and the coastline area are characterized by low V_s velocity, corresponding to the young and poorly consolidated sediments covering these areas. On the other hand, the S-wave velocities are relatively high inside the Falcon Basin, which was uplifted subsequent to being a depocenter in the late Eocene to the middle Miocene (Audemard, 2001; Bezada et al., 2008; Schmitz et al., 2021). The SdP Range, SMU and MA are characterized by high V_s, which is consistent with uplifted crustal rocks. The periphery of the SMM shows a low V_s, reflecting the sedimentary basins to its west and north, with higher velocities in its core. At 5 km depth, most low velocities (V_s < 2.5 km/s) vanish except in the MB. At 18–30 km depth, we observed high V_s beneath the SMM and SdP Range (Figures 6c and 6d). The high velocity at 18 km is ~3.75 km/s, consistent with lower continental or oceanic crustal lithologies (Christensen & Mooney, 1995; Christensen & Salisbury, 1975; Rudnick & Fountain, 1995). At 30 km depth, the high V_s beneath the SMM reaches ~4.2 km/s, indicative of Moho depth.

Beneath the Moho between 43 and 60 km depth are high velocity anomalies that parallel to the coast under the SMM and SdP Range, extend under the SMU to the southwest, and extend from the Guajira Peninsula, under the MB to the MA (Figures 6e and 6f). At 85 km depth, the fast anomalies are much smaller in areal extent, but several appear to vertically connect the shallower high velocities to a large SW-NE striking anomaly at 125 km (Figure 6h). The high velocity anomaly has an S-wave speed ranging from ~4.45 km/s to 4.6 km/s. This deeper

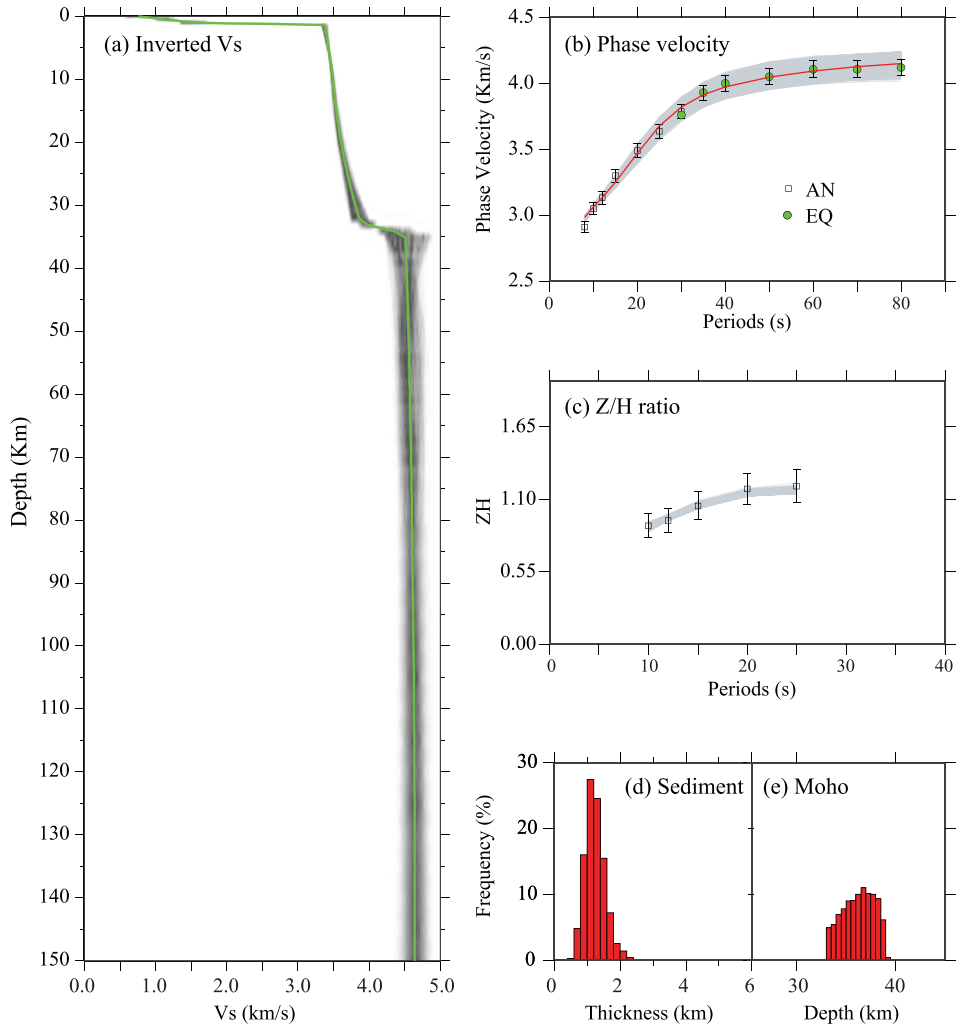

Figure 5. Results of the joint inversion at station CS01 are illustrated as follows: Panel (a) shows the inverted 1-D V_s model, where the shaded area represents the range of all 1,000 accepted models and the green line indicates the average of these models. Panel (b) displays phase velocity fitting, with squares representing measured phase velocities from ambient noise and circles indicating phase velocities from ballistic data. The red line denotes the average dispersion curve of all accepted models, and the shaded area highlights the range of the 1,000 accepted models. Panel (c) presents the same information as (b) but for *Z/H* ratios. Panel (d) shows a histogram of sediment thickness estimates derived from the 1,000 acceptable models. Panel (e) presents a similar histogram for Moho depth.

anomaly aligns with the belt of intermediate depth Bucaramanga nest seismicity (Figure 7. Profile EE′). On the other hand, relatively low velocities underlie the Falcon basin and all but the central MA at all depths.

Figure 7 shows six profiles (AA′, BB′, CC′, DD′, EE′, and FF′) in three different depth ranges corresponding to sedimentary, crustal, and upper mantle structures, respectively. Profile locations are shown in Figure 6h. AA′ and BB′ profiles are in the CAR plate subduction direction (NW-SE direction, Figure 6h). CC′ and DD′ profiles are SW-NE in the strike direction of the MA and the subducted Caribbean slab (Figure 6h). Moho depth is taken as the 4.2 km/s contour. In Figure S4 in Supporting Information S1, we also show the *Vs* perturbations along AA′, BB′, CC′, and DD′.

Profile AA′ runs from the northwestern edge of the SMM to the southern part of the MA. We observe a very low S-wave sediments of the MB and Barinas-Apure Basin (top panel). Beneath the SdP Range and MA, relatively high velocity structures extend from surface to ~20 km depth, indicative of basement uplifts beneath these two mountain ranges. Moho depth increases steadily from 30 km depth below the SMM to ~45 km depth at the

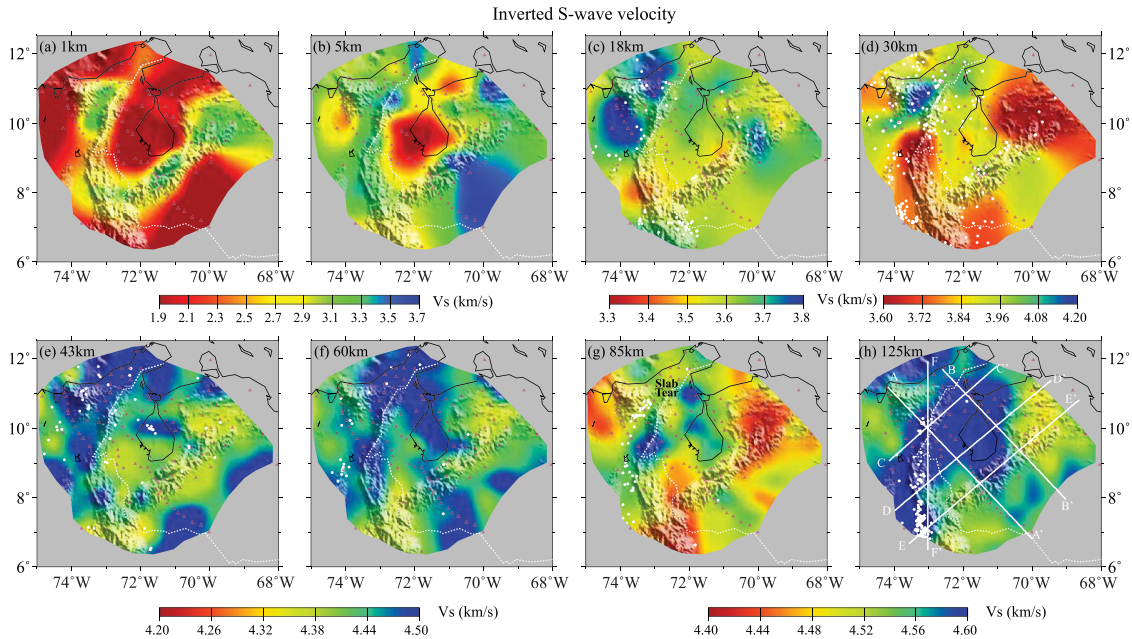

Figure 6. V_s maps at 8 different depths. Panels (a–h) depict the inverted V_s model at depths of 1, 5, 18, 30, 43, 60, 85 km, and 125 km, respectively. Triangles represent the CARMA stations, while white dots indicate local earthquakes obtained from the International Seismological Center and Servicio Geológico Colombiano catalogs.

southeastern edge of MA (middle panel). We observe a high velocity anomaly in the mantle below the SdP Range at ∼90 km depth, dipping toward the southeast along the subduction direction (bottom panel).

Profile BB′ runs through the OAF, MA and extends to the Barinas-Apure Basin. The shallow section in the top reveals low-velocity sediments from the coast to the Barinas-Apure Basin. The middle panel shows that crustal thickness north of the OAF is ∼35 km and changes abruptly to 30 km south of the fault, suggesting that the OAF cuts through the entire crust. Moho depth increases gradually in the inland direction from 30 to ∼40 km depth. We also observe a high velocity anomaly in the depth range of ∼90–150 km above the subducting Caribbean slab (bottom panel).

Profile CC′ runs roughly parallel to the strike of the subducting Caribbean slab, which extends from the Lower Magdalena Valley Basin in the southwest to the Gulf of Venezuela in the northeast. We observe low velocities on either side of the SdP Range that correspond to the Lower Magdalena Valley Basin and the western MB (upper panel). The middle panel indicates that the Moho below the Lower Magdalena Valley Basin and MB is 35–38 km deep, and shallows slightly to ∼32 km beneath the SdP Range. The bottom panel shows a V-shape high velocity anomaly in the upper mantle, which appears to correlate with the intermediate depth subduction seismicity (Cornthwaite et al., 2021). This may suggest that there is a tear or contortion within the Caribbean slab. This structure can also be confirmed in the depth profile FF′ along the N–S direction at 73°W located at the west edge of the tear.

DD′ is another SW-NE profile that runs across the MB and the Falcon Basin. We observe a shallow Moho below the SMU (white line in the middle panel), similar to the Moho depth beneath the SdP Range. The bottom panel shows a high-velocity structure at ∼100–150 km depths below the SMU, which spatially overlaps with the intermediate-depth seismicity of the Bucaramanga nest. At roughly the same depth, there is another high-velocity structure beneath the MB, which lacks seismicity. Low velocity anomalies in the depth range 50–70 km can be seen beneath the SMU and the Falcon Basin.

Profile EE' runs along the strike of the MA. We observe a deeper Moho below the entire range (middle panel), and two low velocity anomalies in the uppermost mantle at either end of the range (bottom panel). In the middle of the range, there is a topographic low, which is underlain by a high velocity anomaly in the depth range of ∼100–150 km (bottom panel).

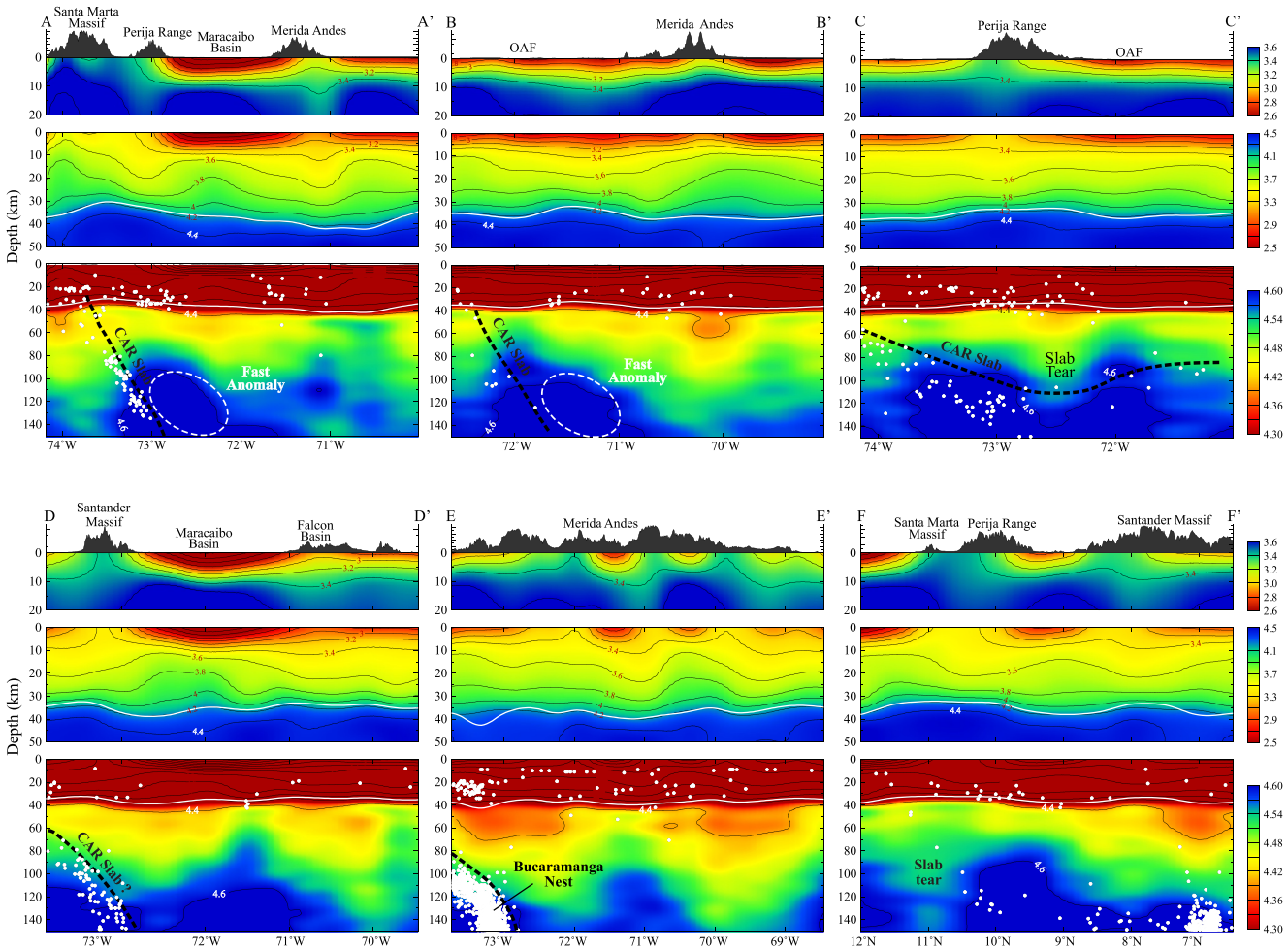

Figure 7. V_s profiles are delineated as white lines in Figure 6h. The top panels display V_s from 0 to 20 km depth, the middle panels show V_s from 0 to 50 km depth, and the bottom panels present V_s from 30 to 150 km depth. Note that the V_s scales differ between each set of panels. The white solid lines represent the Moho depth, while white dots indicate local earthquakes obtained from the International Seismological Center and Servicio Geológico Colombiano catalogs.

4. Discussion

4.1. Sedimentary and Crustal Structures

Figure 8a shows the sediment thickness map in the study area derived from the inversion. We use 2.9 km/s as the basement velocity contour (Li et al., 2021). Understanding 3-D velocity structure of sedimentary basins is of great importance to evaluate seismic hazards as well as to explore natural resources. The MB, bounded by the MA in the southeast, the Falcon Basin in the northeast, and the SdP Range in the northwest, is filled with a large volume of low-velocity sediments from the Cretaceous to Pliocene and occupies most of the Maracaibo block (Audemard, 2001; Bezada et al., 2008; Boschman, 2021; Mann et al., 2006; Schmitz et al., 2021). Its most obvious feature is the ∼9 km sedimentary basin under the Lake Maracaibo, which is consistent with a previous gravity study (Arnaiz-Rodríguez & Audemard, 2014; Kellogg & Bonini, 1982; Sanchez et al., 2011). The Barinas-Apure Basin, formed as a foreland basin by lithospheric flexure and contemporaneous deposition during uplift of the MA, is filled with ∼5 km thick sediments (Audemard & Audemard, 2002; Duerto et al., 2006; Schmitz et al., 2021).

The Lower Magdalena Valley Basin, filled with sediments from the Oligocene to the recent, is the forearc basin associated with oceanic CAR plate subduction under continental SA. Our results suggest that the Lower Magdalena Valley Basin has an average sediment thickness of 4 km, consistent with seismic reflection and well data (Mora-Bohórquez et al., 2017). The Falcon Basin sedimentary units started to accumulate during the Paleocene—

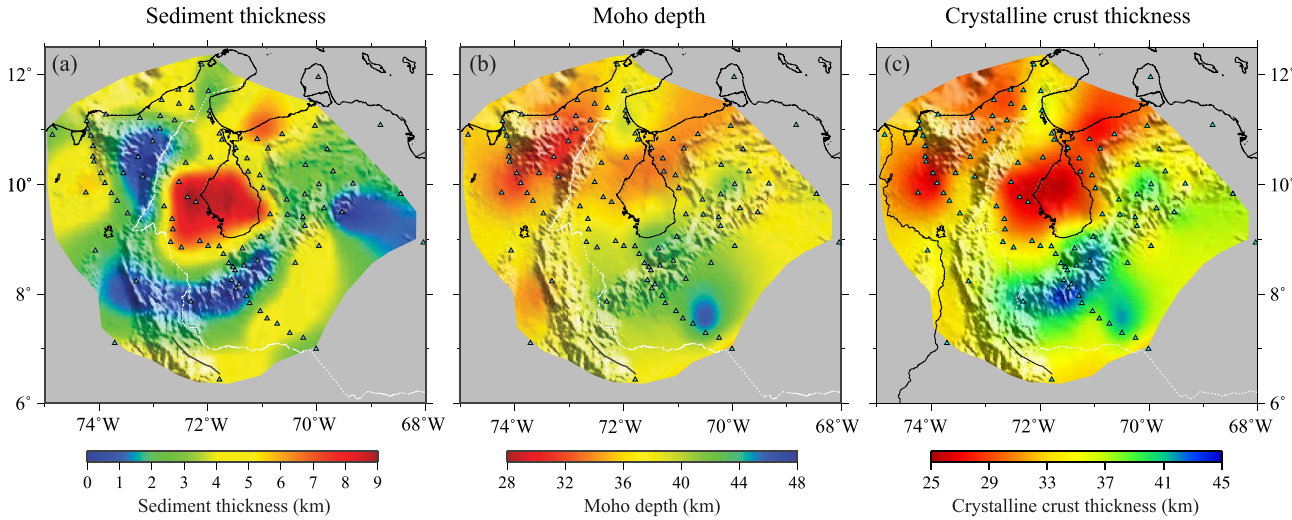

Figure 8. (a) Maps showing sediment thickness, (b) Moho depth, and (c) crystalline crust thickness. Crystalline crust thickness is defined as crustal thickness minus the sediment thickness.

early Eocene, overlying the Caribbean allochthonous basement, with sedimentation ending by the Middle Miocene, as the basin was uplifted to its present elevation of 1,500 m by the compression between the CAR plate and SA plate, forming the Sierra de Falcon (Audemard, 2001; Bezada et al., 2008; Boschman, 2021). The Falcon Basin has an average of ∼3 km thick sediments and is characterized by high Z/H ratios and relatively high V_s (2.5–2.9 km/s).

We define the Moho as the iso-wavespeed surface of the 3-D S-wave velocity model with a proxy of 4.2 km/s. The estimated Moho depth shown in Figure 8b is generally consistent with the results of previous studies (Avila-García et al., 2022; Bezada et al., 2008; Mazuera et al., 2019; Poveda et al., 2018; Schmitz et al., 2021). The Moho depth beneath the SMM is ∼28 km, which is extremely shallow considering its 4 km elevation. This suggests that the elevation is not supported isostatically, but rather dynamically, which is also consistent with gravity data that shows a positive 150 mGal Bouguer anomaly at the SMM (Kellogg & Bonini, 1982).

From the coast region of Colombia in the northwest to the MA in the southeast, Moho depth increases steadily from 25 to 30 km under the SMM to ∼45 km underneath the MA except in the northern part of the Maracaibo block. The Moho depth beneath the SdP Range and southern Maracaibo block is 30–35 km and 35–40 km, respectively. From the BOLIVAR active seismic data (Levander et al., 2006), Bezada et al. (2008) found that the crust thickens from 20 km in the ocean basin to 30+ km beneath the coastal Falcon Basin, and then thins to 27 km under the OAF. Although our data do not extend further north to the profile interpreted by Bezada et al. (2008), we find that the Moho depth beneath the Falcon Basin near the coastline is slightly above 30 km and then increases to 36–40 km toward the south. Further west we do observe abrupt changes in Moho depth across the OAF. There is also a clear separation between the MA and Falcon Basin at the Moho depth, consistent with the receiver function study of BOLIVAR passive source data (Niu et al., 2007). The Moho depth below the Barinas-Apure Basin ranges from 40 to 45 km, which is consistent with the results of active source reflection data of the BOLIVAR and GEODINOS projects (Bezada et al., 2008). In Figure 8c, we calculate the crystalline crust thickness by first adding the elevation to the Moho depth to obtain crustal thickness, and then subtracting sediment from crustal thickness. The thinnest crystalline crust (∼25 km) is located beneath the MB, which may suggest that it is formed by extension prior to the current tectonic activity. The downwarping of the MB could be caused by the falling CLIP that partly attached to the east part of the basin, as discussed below.

4.2. Slab Rollback and CLIP Falloff

To better understand the nature of the high velocity anomalies above the slab, we show volumes of high and low velocity anomalies of our 3-D velocity model in the upper mantle (Figure 9). The high velocity anomalies above the subducting Caribbean slab shown in the depth maps (Figure 6) and cross sections are actually connected

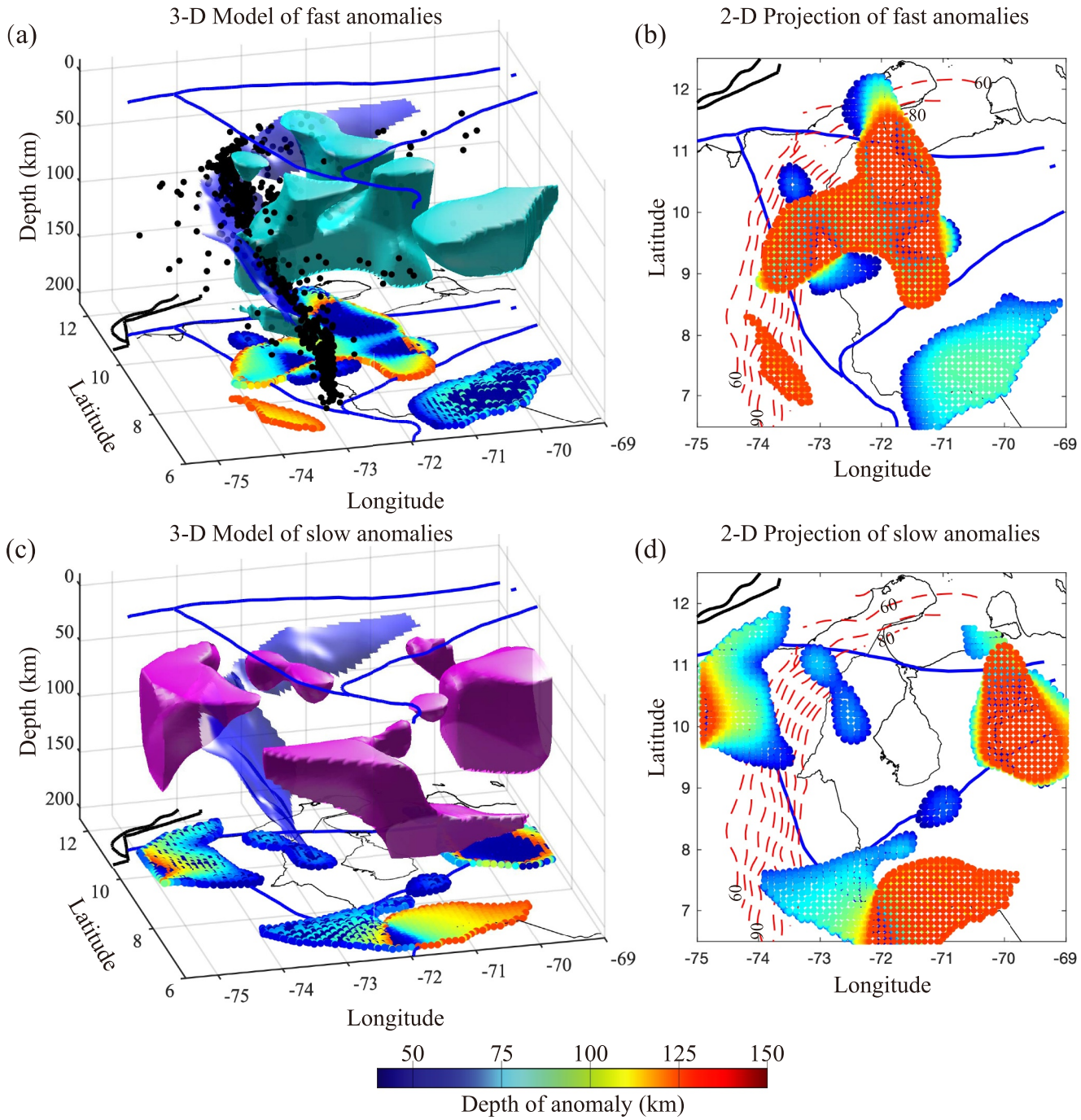

Figure 9. 3-D view of fast and slow anomalies obtained from the inverted V_s model. Panel (a) shows the 3-D view of fast anomalies, with the cyan isosurface representing 1% fast anomalies. The blue surface indicates the top of the CAR, determined by local seismicity (Cornthwaite et al., 2021). Panel (b) presents a map view projection of the fast anomalies. Panels (c) and (d) are the same as (a) and (b), respectively, but for slow anomalies.

(Figure 7a). The S-wave velocity of the volume ranges from ~4.5 km/s at 70 km depth to 4.6 km/s above the slab surface. Beneath the SdP Range and western part of the MB, the high velocity body appears to be detached from the crust, while it appears at the base of the crust beneath the eastern part of the MB (Figure 9a). In Figure 9b, the orange hatched area illustrates the 2-D surface projection of the high-velocity body. The high velocity looks like a letter *T* tilted to the right side. The top part is located at the base of the crust under most of the eastern MB beneath Lake Maracaibo, while its leg is deeper in the mantle, a scenario that suggests delamination. Based on its location

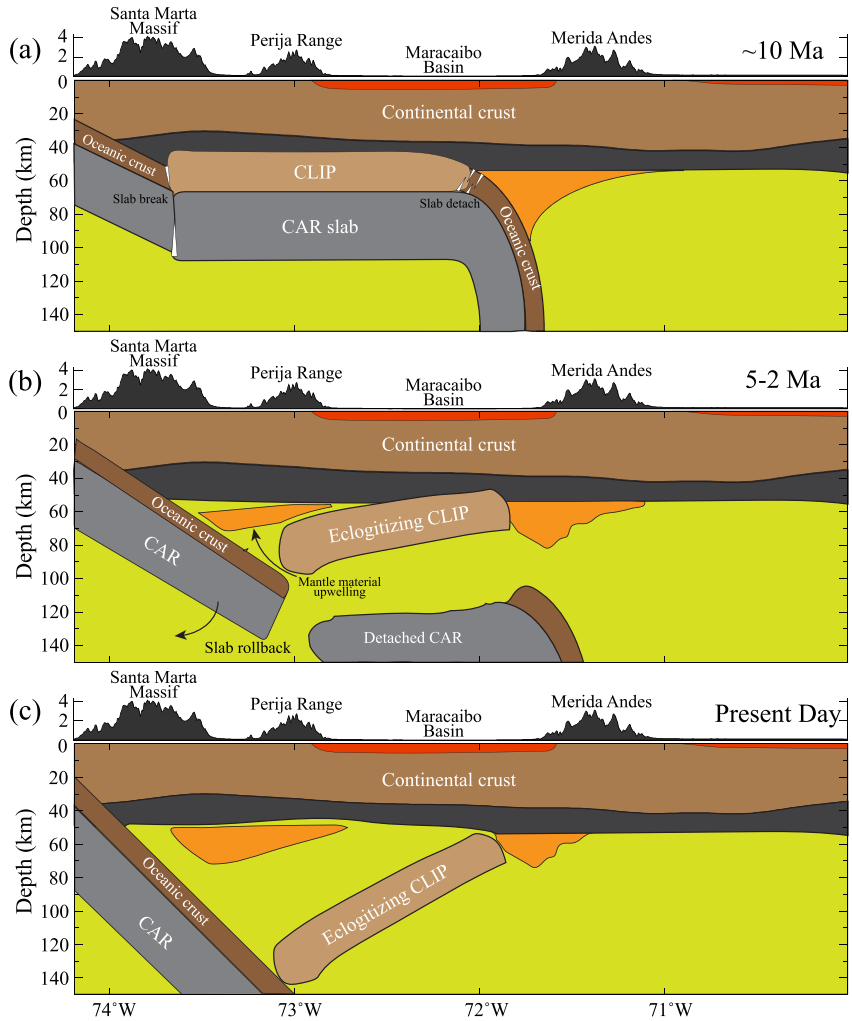

Figure 10. A 2-D schematic model illustrating the scenario of Caribbean large igneous province falling from the overriding Maracaibo block and the recent episode of rollback of the Caribbean slab.

and geometry, we speculate that the high velocity anomaly is a piece of formerly subducted CLIP after eclogitization. Generally, eclogites exhibit slightly higher shear wave velocities (V_s) compared to peridotites at 3.0 GPa and 750°C, with weaker anisotropy (Worthington et al., 2013). Its positive buoyancy caused it to subduct flatly underneath the Maracaibo block and attached below the MA block. Numerical modeling suggested that flat slabs can erode the lowermost continental mantle lithosphere, and fill the space normally occupied by the subduction mantle wedge, preventing arc-type melting (e.g., Axen et al., 2018; McQuarrie & Chase, 2000). Since 45 Ma, the CAR-SA subduction zone has had little volcanism but has experienced uplift of the SMM, the SdP Range, and the MA (Kellogg & Bonini, 1982).

Cornthwaite et al. (2021) imaged the subducting Caribbean slab in the upper mantle with finite frequency teleseismic P-wave tomography and identified a detached segment of the subducted CAR plate. They inferred that a slab break-off event occurred at ~10 Ma, contemporaneously with the uplift of the MA. The detached slab is parallel to and below the current MA at 200 km depth. We hypothesize that slab breakoff caused the subduction zone to jump westward, leaving the CLIP underlying Maracaibo. Subduction transferred from flat to normal subduction and triggered slab rollback. The warm return flow generated by the normal subduction process facilitates the eclogitization of the flat lying CLIP (H. Wang et al., 2021). Subsequent eclogitization leads to the development of a negative buoyancy. As a result, the flat lying CLIP peels off from the overlying plate at its western end beneath the SdP Range and descends onto the subducting CAR plate. However, its eastern end is still

attached to the overlying plate beneath the eastern part of the MB. This hypothesis also explains much of the irregular geometry of high velocity anomalies between the Moho underneath the Maracaibo block and the currently subducting CAR plate.

We summarize the model in the schematic Figure 10. As the CLIP subducts at a shallow angle beneath the Maracaibo block, it erodes the lowermost Maracaibo block lithosphere and couples with the overriding plate. Due to its positive buoyancy, the CLIP accreted to the base of the Maracaibo block (Figure 10a). At ∼10 Ma, the deep part of the subducted Caribbean slab detached, and the subduction zone jumped westward and established a normal subduction angle (Cornthwaite et al., 2021). Subsequently, the flat lying CLIP was exposed to higher temperatures and pressures and began to eclogitize (Figure 10b). Since the negative buoyancy of the eclogitized CLIP started to detach from the overlying plate and descend on to the subducting CAR (Figure 10c). It should be noticed that the imaged high-velocity anomalies shown in Figure 9 predominantly reside above the subducting slab and possess a complex 3-D configuration. Because of the complex geometry, a 2-D schematic model cannot capture all aspects, though it aims to represent the key processes driving the formation of the major high-velocity body.

4.3. Slab Tear Within the Caribbean Plate

In Figure 7 profile CC′ and FF′, we observe noticeable discontinuities both in high velocity anomalies and seismicity. In profile CC′, there is a V-shape low velocity anomaly beneath the SdP Range at depths of 60–140 km and the mantle seismicity is consistent with a high velocity (∼4.6 km/s) subducting slab. In profile FF′, we observe the discontinuity of both low velocity anomaly and an abrupt end to most intermediate-depth seismicity at the tip of the V.

The 3-D volume of the slow anomalies (Figure 9c) and their 2-D projection (Figure 9d) suggest two large low-velocity bodies beneath the northeast and southwest ends of the MA. Masy et al. (2011) measured shear wave splitting from SKS waveform data recorded by 23 broadband seismic stations in western Venezuela, and found splitting parallel to the MA, with a rapid change in fast polarization direction at ∼10.5°N and large splitting time at coastal stations. They speculated that there is a tear in the subducting Caribbean slab which runs east west from the SdP Range at ∼10.5°N or further north and extends to ∼71.5°W, which agrees well with the location of the V-shape in Figure CC′.

5. Conclusions

In this paper, we jointly inverted ambient noise Rayleigh wave *Z*/*H* ratios, phase velocities in the 8–30 s band and ballistic Rayleigh wave phase velocities in 30–80 s band to construct a 3-D S-wave velocity model in the area from 75°–65°W to 5°–12°N. We found a westward dipping high velocity body beneath the SdP Range and MB above the subducting CAR plate and speculated that it is a piece of flat subducted CLIP detaching from the overlying plate. We observed a high velocity gap along the strike of the subducting Caribbean slab beneath the northern SdP Range near station ML01 (Figure 1). Combining the intermediate-depth seismicity and SKS splitting data, we suggested that there is a tear within the subducting Caribbean slab underneath the northern SdP Range. We found that the eastern MB has the thinnest crystalline crust and inferred that the downwarping of the MB is likely caused by the pull of falling CLIP as well as the compression between the Caribbean and South American plates.

Data Availability Statement

Broadband seismic records collected on the 65 IRIS-PASSCAL stations are available through the IRIS Data Management Center via Levander (2016). Data collected on Venezuelan instruments are available by request through the FUNVISIS agency (servicios@funvisis.gob.ve). Data collected on Servicio Geològico Colombiano instruments are freely available and accessible to the scientific community through written request and justification addressed to the Colombian Geological Survey (sismologo@sgc.gov.co).

Acknowledgments
We thank all the people involved in the CARMA Array project for installing and servicing the seismic array, Fundación de Investigaciones Simológicas (FUNVISIS) of Venezuela and [5]Servicio Geológico Colombiano for providing their national seismic network data. We thank Dr. Hongrui Qiu for his suggestions on the inversion strategy. We are grateful to the Editor, Dr. Anne Paul, Dr. Franck A. Audemard, and an anonymous reviewer for providing very thoughtful and constructive reviews that improved the manuscript significantly. The CARMA project was supported by the National Science Foundation (Grant EAR 1459047). W.M. is supported by the Special Fund of the Institute of Geophysics, China Earthquake Administration (Grant DQJB23R28), the National Natural Science Foundation of China (Grants 42304078, U1839210, and 42104043).

References

Afonso, J. C., Fullea, J., Griffin, W. L., Yang, Y., Jones, A. G., D. Connolly, J. A., & O'Reilly, S. Y. (2013). 3-D multiobservable probabilistic inversion for the compositional and thermal structure of the lithosphere and upper mantle. I: A priori petrological information and geophysical observables. *Journal of Geophysical Research: Solid Earth*, *118*(5), 2586–2617. https://doi.org/10.1002/jgrb.50124

Arnaiz-Rodríguez, M. S., & Audemard, F. (2014). Variations in elastic thickness and flexure of the Maracaibo block. *Journal of South American Earth Sciences*, *56*, 251–264. https://doi.org/10.1016/j.jsames.2014.09.014

Audemard, F. A. (2001). Quaternary tectonics and present stress tensor of the inverted northern Falcón Basin, northwestern Venezuela. *Journal of Structural Geology*, *23*(2–3), 431–453. https://doi.org/10.1016/S0191-8141(00)00116-4

Audemard, F. A. (2003). Geomorphic and geologic evidence of ongoing uplift and deformation in the Mérida Andes, Venezuela. *Quaternary International*, *101–102*, 43–65. https://doi.org/10.1016/S1040-6182(02)00128-3

Audemard, F. A. (2009). Key issues on the post-Mesozoic southern Caribbean plate boundary. *Geological Society, London, Special Publications*, *328*(1), 569–586. https://doi.org/10.1144/SP328.23

Audemard, F. A. (2014). Active block tectonics in and around the Caribbean: A review. In M. Schmitz, F. A. Audemard, & F. Urbani (Eds.), *El Límite Noreste de la Placa Suramericana - Estructuras Litosféricas de la Superficie al Manto (The Northeastern Limit of the South American Plate - Lithospheric Structures from Surface to the Mantle) Editorial Innovación Tecnológica*. Facultad de Ingeniería-Universidad Central de Venezuela/FUNVISIS.

Audemard, F. A., & Castilla, R. (2016). Present-day stress tensors along the southern Caribbean plate boundary zone from inversion of focal mechanism solutions: A successful trial. *Journal of South American Earth Sciences*, *71*, 309–319. https://doi.org/10.1016/j.jsames.2016.06.005

Audemard, F. A., Romero, G., Rendon, H., & Cano, V. (2005). Quaternary fault kinematics and stress tensors along the southern Caribbean from fault-slip data and focal mechanism solutions. *Earth-Science Reviews*, *69*(3–4), 181–233. https://doi.org/10.1016/j.earscirev.2004.08.001

Audemard, F. E., & Audemard, F. A. (2002). Structure of the Mérida Andes, Venezuela: Relations with the South America–Caribbean geodynamic interaction. *Tectonophysics*, *345*(1–4), 1–26. https://doi.org/10.1016/S0040-1951(01)00218-9

Avila-García, J., Schmitz, M., Mortera-Gutierrez, C., Bandy, W., Yegres, L., Zelt, C., & Aray-Castellano, J. (2022). Crustal structure and tectonic implications of the southernmost Merida Andes, Venezuela, from wide-angle seismic data analysis. *Journal of South American Earth Sciences*, *116*, 103853. https://doi.org/10.1016/j.jsames.2022.103853

Axen, G. J., Van Wijk, J. W., & Currie, C. A. (2018). Basal continental mantle lithosphere displaced by flat-slab subduction. *Nature Geoscience*, *11*(12), 961–964. https://doi.org/10.1038/s41561-018-0263-9

Barazangi, M., & Isacks, B. L. (1976). Spatial distribution of earthquakes and subduction of the Nazca plate beneath South America. *Geology*, *4*(11), 686. https://doi.org/10.1130/0091-7613(1976)4<686:SDOEAS>2.0.CO;2

Barrera-Lopez, C. V., Mooney, W. D., & Kaban, M. K. (2022). Regional geophysics of the Caribbean and northern South America: Implications for tectonics. *Geochemistry, Geophysics, Geosystems*, *23*(5), e2021GC010112. https://doi.org/10.1029/2021GC010112

Ben-Avraham, Z., Nur, A., Jones, D., & Cox, A. (1981). Continental accretion: From oceanic plateaus to allochthonous terranes. *Science*, *213*(4503), 47–54. https://doi.org/10.1126/science.213.4503.47

Bensen, G. D., Ritzwoller, M. H., Barmin, M. P., Levshin, A. L., Lin, F., Moschetti, M. P., et al. (2007). Processing seismic ambient noise data to obtain reliable broad-band surface wave dispersion measurements. *Geophysical Journal International*, *169*(3), 1239–1260. https://doi.org/10.1111/j.1365-246X.2007.03374.x

Bezada, M. J., Levander, A., & Schmandt, B. (2010). Subduction in the southern Caribbean: Images from finite-frequency P wave tomography. *Journal of Geophysical Research*, *115*(B12), 2010JB007682. https://doi.org/10.1029/2010JB007682

Bezada, M. J., Schmitz, M., Jácome, M. I., Rodríguez, J., Audemard, F., & Izarra, C. (2008). Crustal structure in the Falcón Basin area, northwestern Venezuela, from seismic and gravimetric evidence. *Journal of Geodynamics*, *45*(4–5), 191–200. https://doi.org/10.1016/j.jog.2007.11.002

Bilham, R. G., & Mencin, D. (2013). Potential for Great Thrust Earthquakes in NE Colombia & NW Venezuela, 2013, T21A-01. In *Presented at the AGU Spring Meeting Abstracts*.

Bird, P. (1988). Formation of the Rocky Mountains, western United States: A continuum computer model. *Science*, *239*(4847), 1501–1507. https://doi.org/10.1126/science.239.4847.1501

Bishop, B. T., Beck, S. L., Zandt, G., Wagner, L., Long, M., Antonijevic, S. K., et al. (2017). Causes and consequences of flat-slab subduction in southern Peru. *Geosphere*, *13*(5), 1392–1407. https://doi.org/10.1130/GES01440.1

Bodin, T., Sambridge, M., Gallagher, K., & Rawlinson, N. (2012). Transdimensional inversion of receiver functions and surface wave dispersion. *Journal of Geophysical Research*, *117*(B2), 2011JB008560. https://doi.org/10.1029/2011JB008560

Boschman, L. M. (2021). Andean mountain building since the Late Cretaceous: A paleoelevation reconstruction. *Earth-Science Reviews*, *220*, 103640. https://doi.org/10.1016/j.earscirev.2021.103640

Brocher, T. M. (2005). Empirical relations between elastic wavespeeds and density in the Earth's crust. *Bulletin of the Seismological Society of America*, *95*(6), 2081–2092. https://doi.org/10.1785/0120050077

Cardona, A., Valencia, V. A., Bayona, G., Duque, J., Ducea, M., Gehrels, G., et al. (2011). Early-subduction-related orogeny in the northern Andes: Turonian to Eocene magmatic and provenance record in the Santa Marta Massif and Rancheria Basin, northern Colombia. *Terra Nova*, *23*(1), 26–34. https://doi.org/10.1111/j.1365-3121.2010.00979.x

Christensen, N. I., & Mooney, W. D. (1995). Seismic velocity structure and composition of the continental crust: A global view. *Journal of Geophysical Research*, *100*(B6), 9761–9788. https://doi.org/10.1029/95JB00259

Christensen, N. I., & Salisbury, M. H. (1975). Structure and constitution of the lower oceanic crust. *Reviews of Geophysics*, *13*(1), 57–86. https://doi.org/10.1029/RG013i001p00057

Colmenares, L., & Zoback, M. D. (2003). Stress field and seismotectonics of northern South America. *Geology*, *31*(8), 721. https://doi.org/10.1130/G19409.1

Cornthwaite, J., Bezada, M. J., Miao, W., Schmitz, M., Prieto, G. A., Dionicio, V., et al. (2021). Caribbean Slab segmentation beneath northwest South America revealed by 3-D finite frequency teleseismic P-wave tomography. *Geochemistry, Geophysics, Geosystems*, *22*(4), e2020GC009431. https://doi.org/10.1029/2020GC009431

De Toni, B., & Kellogg, J. (1993). Seismic evidence for blind thrusting of the northwestern flank of the Venezuelan Andes. *Tectonics*, *12*(6), 1393–1409. https://doi.org/10.1029/93TC01893

Duerto, L., Escalona, A., & Mann, P. (2006). Deep structure of the Mérida Andes and Sierra de Perijá mountain fronts, Maracaibo Basin, Venezuela. *AAPG Bulletin*, *90*(4), 505–528. https://doi.org/10.1306/10080505033

Dziewonski, A., Bloch, S., & Landisman, M. (1969). A technique for the analysis of transient seismic signals. *Bulletin of the Seismological Society of America*, *59*(1), 427–444. https://doi.org/10.1785/BSSA0590010427

Dziewonski, A. M., & Anderson, D. L. (1981). Preliminary reference Earth model. *Physics of the Earth and Planetary Interiors*, *25*(4), 297–356. https://doi.org/10.1016/0031-9201(81)90046-7

Eakin, C. M., Long, M. D., Beck, S. L., Wagner, L. S., Tavera, H., & Condori, C. (2014). Response of the mantle to flat slab evolution: Insights from local *S* splitting beneath Peru. *Geophysical Research Letters*, *41*(10), 3438–3446. https://doi.org/10.1002/2014GL059943

Escalona, A., & Mann, P. (2006). Tectonic controls of the right-lateral Burro Negro tear fault on Paleogene structure and stratigraphy, northeastern Maracaibo Basin. *AAPG Bulletin*, *90*(4), 479–504. https://doi.org/10.1306/10070505032

Forsyth, D. W., & Li, A. (2005). Array analysis of two-dimensional variations in surface wave phase velocity and azimuthal anisotropy in the presence of multipathing interference. In A. Levander & G. Nolet (Eds.), *Geophysical Monograph Series* (Vol. 157, pp. 81–97). American Geophysical Union. https://doi.org/10.1029/157GM06

Gardner, G. H. F., Gardner, L. W., & Gregory, A. R. (1974). Formation velocity and density—The diagnostic basics for stratigraphic traps. *Geophysics*, *39*(6), 770–780. https://doi.org/10.1190/1.1440465

Gutscher, M., Spakman, W., Bijwaard, H., & Engdahl, E. R. (2000). Geodynamics of flat subduction: Seismicity and tomographic constraints from the Andean margin. *Tectonics*, *19*(5), 814–833. https://doi.org/10.1029/1999TC001152

Herrmann, R. B., & Ammon, C. J. (2004). *Surface waves, receiver functions and crustal structure*, *Computer Programs in Seismology, Version 3.30*. Saint Louis University. Retrieved from http://www.eas.slu.edu/eqc/eqc_cps/CPS/CPS330/cps330c.pdf

Hilst, R. V. D., & Mann, P. (1994). Tectonic implications of tomographic images of subducted lithosphere beneath northwestern South America. *Geology*, *22*(5), 451. https://doi.org/10.1130/0091-7613(1994)022<0451:TIOTIO>2.3.CO;2

Hippolyte, J.-C., & Mann, P. (2011). Neogene–Quaternary tectonic evolution of the Leeward Antilles islands (Aruba, Bonaire, Curaçao) from fault kinematic analysis. *Marine and Petroleum Geology*, *28*(1), 259–277. https://doi.org/10.1016/j.marpetgeo.2009.06.010

Humphreys, E., Hessler, E., Dueker, K., Farmer, G. L., Erslev, E., & Atwater, T. (2003). How Laramide-age hydration of North American lithosphere by the Farallon slab controlled subsequent activity in the western United States. *International Geology Review*, *45*(7), 575–595. https://doi.org/10.2747/0020-6814.45.7.575

Jordan, T. E., & Allmendinger, R. W. (1986). The Sierras Pampeanas of Argentina; a modern analogue of Rocky Mountain foreland deformation. *American Journal of Science*, *286*(10), 737–764. https://doi.org/10.2475/ajs.286.10.737

Kay, S. M., Maksaev, V., Moscoso, R., Mpodozis, C., & Nasi, C. (1987). Probing the evolving Andean Lithosphere: Mid-Late Tertiary magmatism in Chile (29°–30°30′S) over the modern zone of subhorizontal subduction. *Journal of Geophysical Research*, *92*(B7), 6173–6189. https://doi.org/10.1029/JB092iB07p06173

Kellogg, J. N. (1984). Cenozoic tectonic history of the Sierra de Perijá, Venezuela-Colombia, and adjacent basins. In *Geological Society of America Memoirs* (Vol. 162, pp. 239–262). Geological Society of America. https://doi.org/10.1130/MEM162-p239

Kellogg, J. N., & Bonini, W. E. (1982). Subduction of the Caribbean Plate and basement uplifts in the overriding South American Plate. *Tectonics*, *1*(3), 251–276. https://doi.org/10.1029/TC001i003p00251

Levander, A. (2016). *Caribbean-Merida Andes experiment*. International Federation of Digital Seismograph Networks. https://doi.org/10.7914/SN/YU_2016

Levander, A., Schmitz, M., Avé Lallemant, H. G., Zelt, C. A., Sawyer, D. S., Magnani, M. B., et al. (2006). Evolution of the southern Caribbean plate boundary. *Eos, Transactions American Geophysical Union*, *87*(9), 97–100. https://doi.org/10.1029/2006EO090001

Levshin, A. L., & Ritzwoller, M. H. (2001). Automated detection, extraction, and measurement of regional surface waves. *Pure and Applied Geophysics*, *158*(8), 1531–1545. https://doi.org/10.1007/PL00001233

Li, G., Chen, H., Niu, F., Guo, Z., Yang, Y., & Xie, J. (2016). Measurement of Rayleigh wave ellipticity and its application to the joint inversion of high-resolution S wave velocity structure beneath northeast China. *Journal of Geophysical Research: Solid Earth*, *121*(2), 864–880. https://doi.org/10.1002/2015JB012459

Li, G., Niu, F., Yang, Y., & Xie, J. (2018). An investigation of time–frequency domain phase-weighted stacking and its application to phase-velocity extraction from ambient noise's empirical Green's functions. *Geophysical Journal International*, *212*(2), 1143–1156. https://doi.org/10.1093/gji/ggx448

Li, G., Yang, Y., Niu, F., & Chen, M. (2021). 3-D sedimentary structures beneath southeastern Australia constrained by passive seismic array data. *Journal of Geophysical Research: Solid Earth*, *126*(2), e2020JB019998. https://doi.org/10.1029/2020JB019998

Lin, F.-C., Schmandt, B., & Tsai, V. C. (2012). Joint inversion of Rayleigh wave phase velocity and ellipticity using USArray: Constraining velocity and density structure in the upper crust. *Geophysical Research Letters*, *39*(12), L12303. https://doi.org/10.1029/2012GL052196

Lin, F.-C., Tsai, V. C., & Schmandt, B. (2014). 3-D crustal structure of the western United States: Application of Rayleigh-wave ellipticity extracted from noise cross-correlations. *Geophysical Journal International*, *198*(2), 656–670. https://doi.org/10.1093/gji/ggu160

Macellari, C. E. (1995). Cenozoic sedimentation and tectonics of the southwestern Caribbean pull-apart basin, Venezuela and Colombia. In A. J. Tankard, R. Suárez Soruco, & H. J. Welsink (Eds.), *Petroleum Basins of South America* (Vol. 62). AAPG Memoir. https://doi.org/10.1306/M62593

Mann, P., Escalona, A., & Verónica, M. (2006). Regional geologic and tectonic setting of the Maracaibo supergiant basin, western Venezuela. *AAPG Bulletin*, *90*(4), 445–477. https://doi.org/10.1306/10110505031

Masy, J., Niu, F., Levander, A., & Schmitz, M. (2011). Mantle flow beneath northwestern Venezuela: Seismic evidence for a deep origin of the Mérida Andes. *Earth and Planetary Science Letters*, *305*(3–4), 396–404. https://doi.org/10.1016/j.epsl.2011.03.024

Masy, J., Niu, F., Levander, A., & Schmitz, M. (2015). Lithospheric expression of Cenozoic subduction, mesozoic rifting and the Precambrian Shield in Venezuela. *Earth and Planetary Science Letters*, *410*, 12–24. https://doi.org/10.1016/j.epsl.2014.08.041

Mazuera, F., Schmitz, M., Escalona, A., Zelt, C., & Levander, A. (2019). Lithospheric structure of northwestern Venezuela from wide-angle seismic data: Implications for the understanding of continental margin evolution. *Journal of Geophysical Research: Solid Earth*, *124*(12), 13124–13149. https://doi.org/10.1029/2019JB017892

McQuarrie, N., & Chase, C. G. (2000). Raising the Colorado Plateau. *Geology*, *28*(1), 91–94. https://doi.org/10.1130/0091-7613(2000)028<0091:RTCP>2.3.CO;2

Miao, W., Niu, F., Li, G., & Levander, A. (2022). Sedimentary and crustal structure of the US Gulf Coast revealed by Rayleigh wave and teleseismic P coda data with implications for continent rifting. *Earth and Planetary Science Letters*, *577*, 117257. https://doi.org/10.1016/j.epsl.2021.117257

Montes, C., Rodriguez-Corcho, A. F., Bayona, G., Hoyos, N., Zapata, S., & Cardona, A. (2019). Continental margin response to multiple arc-continent collisions: The northern Andes-Caribbean margin. *Earth-Science Reviews*, *198*, 102903. https://doi.org/10.1016/j.earscirev.2019.102903

Mora, J. A., Oncken, O., Le Breton, E., Ibánez-Mejia, M., Faccenna, C., Veloza, G., et al. (2017). Linking Late Cretaceous to Eocene tectonostratigraphy of the San Jacinto fold belt of NW Colombia with Caribbean plateau collision and flat subduction. *Tectonics*, *36*(11), 2599–2629. https://doi.org/10.1002/2017TC004612

Mora-Bohórquez, J. A., Ibánez-Mejia, M., Oncken, O., De Freitas, M., Vélez, V., Mesa, A., & Serna, L. (2017). Structure and age of the Lower Magdalena Valley basin basement, northern Colombia: New reflection-seismic and U-Pb-Hf insights into the termination of the central Andes against the Caribbean basin. *Journal of South American Earth Sciences*, *74*, 1–26. https://doi.org/10.1016/j.jsames.2017.01.001

Niu, F., Bravo, T., Pavlis, G., Vernon, F., Rendon, H., Bezada, M., & Levander, A. (2007). Receiver function study of the crustal structure of the southeastern Caribbean plate boundary and Venezuela. *Journal of Geophysical Research*, *112*(B11), 2006JB004802. https://doi.org/10.1029/2006JB004802

Pennington, W. D. (1981). Subduction of the eastern Panama Basin and seismotectonics of northwestern South America. *Journal of Geophysical Research*, *86*(B11), 10753–10770. https://doi.org/10.1029/JB086iB11p10753

Poveda, E., Julià, J., Schimmel, M., & Perez-Garcia, N. (2018). Upper and middle crustal velocity structure of the Colombian Andes from ambient noise tomography: Investigating subduction-related magmatism in the overriding plate. *Journal of Geophysical Research: Solid Earth*, *123*(2), 1459–1485. https://doi.org/10.1002/2017JB014688

Ramos, V. A., Cristallini, E. O., & Pérez, D. J. (2002). The Pampean flat-slab of the Central Andes. *Journal of South American Earth Sciences*, *15*(1), 59–78. https://doi.org/10.1016/S0895-9811(02)00006-8

Ramos, V. A., & Folguera, A. (2009). Andean flat-slab subduction through time. *Geological Society, London, Special Publications*, *327*(1), 31–54. https://doi.org/10.1144/SP327.3

Rudnick, R. L., & Fountain, D. M. (1995). Nature and composition of the continental crust: A lower crustal perspective. *Reviews of Geophysics*, *33*(3), 267–309. https://doi.org/10.1029/95RG01302

Sanchez, J., Götze, H.-J., & Schmitz, M. (2011). A 3-D lithospheric model of the Caribbean-South American plate boundary. *International Journal of Earth Sciences*, *100*(7), 1697–1712. https://doi.org/10.1007/s00531-010-0600-8

Sandwell, D. T., & Smith, W. H. F. (2009). Global marine gravity from retracked Geosat and ERS-1 altimetry: Ridge segmentation versus spreading rate. *Journal of Geophysical Research*, *114*(B1), 2008JB006008. https://doi.org/10.1029/2008JB006008

Schmitz, M., Ramírez, K., Mazuera, F., Ávila, J., Yegres, L., Bezada, M., & Levander, A. (2021). Moho depth map of northern Venezuela based on wide-angle seismic studies. *Journal of South American Earth Sciences*, *107*, 103088. https://doi.org/10.1016/j.jsames.2020.103088

Schubert, C. (1982). Origin of Cariaco Basin, southern Caribbean Sea. *Marine Geology*, *47*(3–4), 345–360. https://doi.org/10.1016/0025-3227(82)90076-7

Shen, W., Ritzwoller, M. H., & Schulte-Pelkum, V. (2013). A 3-D model of the crust and uppermost mantle beneath the Central and Western US by joint inversion of receiver functions and surface wave dispersion. *Journal of Geophysical Research: Solid Earth*, *118*(1), 262–276. https://doi.org/10.1029/2012JB009602

Sun, M., Bezada, M. J., Cornthwaite, J., Prieto, G. A., Niu, F., & Levander, A. (2022). Overlapping slabs: Untangling subduction in NW South America through finite-frequency teleseismic tomography. *Earth and Planetary Science Letters*, *577*, 117253. https://doi.org/10.1016/j.epsl.2021.117253

Symithe, S., Calais, E., de Chabalier, J. B., Robertson, R., & Higgins, M. (2015). Current block motions and strain accumulation on active faults in the Caribbean. *Journal of Geophysical Research: Solid Earth*, *120*(5), 3748–3774. https://doi.org/10.1002/2014JB011779

Syracuse, E. M., Maceira, M., Prieto, G. A., Zhang, H., & Ammon, C. J. (2016). Multiple plates subducting beneath Colombia, as illuminated by seismicity and velocity from the joint inversion of seismic and gravity data. *Earth and Planetary Science Letters*, *444*, 139–149. https://doi.org/10.1016/j.epsl.2016.03.050

Taboada, A., Rivera, L. A., Fuenzalida, A., Cisternas, A., Philip, H., Bijwaard, H., et al. (2000). Geodynamics of the northern Andes: Subductions and intracontinental deformation (Colombia). *Tectonics*, *19*(5), 787–813. https://doi.org/10.1029/2000TC900004

Van Benthem, S., Govers, R., Spakman, W., & Wortel, R. (2013). Tectonic evolution and mantle structure of the Caribbean. *Journal of Geophysical Research: Solid Earth*, *118*(6), 3019–3036. https://doi.org/10.1002/jgrb.50235

Wang, C., Gordon, R. G., Zhang, T., & Zheng, L. (2019). Observational test of the global moving hot spot reference frame. *Geophysical Research Letters*, *46*(14), 8031–8038. https://doi.org/10.1029/2019GL083663

Wang, H., Currie, C. A., & DeCelles, P. G. (2021). Coupling between lithosphere removal and mantle flow in the Central Andes. *Geophysical Research Letters*, *48*(16), e2021GL095075. https://doi.org/10.1029/2021GL095075

Worthington, J. R., Hacker, B. R., & Zandt, G. (2013). Distinguishing eclogite from peridotite: EBSD-based calculations of seismic velocities. *Geophysical Journal International*, *193*(1), 489–505. https://doi.org/10.1093/gji/ggt004

Yang, Y., & Forsyth, D. W. (2006a). Rayleigh wave phase velocities, small-scale convection, and azimuthal anisotropy beneath southern California. *Journal of Geophysical Research*, *111*(B7), 2005JB004180. https://doi.org/10.1029/2005JB004180

Yang, Y., & Forsyth, D. W. (2006b). Regional tomographic inversion of the amplitude and phase of Rayleigh waves with 2-D sensitivity kernels. *Geophysical Journal International*, *166*(3), 1148–1160. https://doi.org/10.1111/j.1365-246X.2006.02972.x

Zhang, T., Gordon, R. G., Mishra, J. K., & Wang, C. (2017). The Malpelo plate hypothesis and implications for nonclosure of the Cocos-Nazca-Pacific plate motion circuit. *Geophysical Research Letters*, *44*(16), 8213–8218. https://doi.org/10.1002/2017GL073704